Available online at www.sciencedirect.com

SCIENCE DIRECT®

Earth and Planetary Science Letters 235 (2005) 361–374

EPSL

www.elsevier.com/locate/epsl

Gouge formation by dynamic pulverization during earthquake rupture

Ze'ev Reches*, Thomas A. Dewers

School of Geology and Geophysics, University of Oklahoma, Norman OK, 73019, USA

Received 29 December 2004; received in revised form 30 March 2005; accepted 8 April 2005
Available online 31 May 2005
Editor: Scott King

Abstract

It is proposed here that fault gouge forms by rock pulverization within the tip region of a fast propagating earthquake due to the intensity of stress and rates of strain in this zone. To examine this mechanism, we calculate the deformation conditions of a dynamic shear fracture propagating close to the limiting Rayleigh wave velocity. The mechanical conditions close to the fracture tip are extreme: tensile stresses approach 5 GPa, volumetric strain rates exceed 10^5 s^{-1}, and volumetric expansion alternates with volumetric contraction. It is expected that a localized zone a few millimeters wide will be pulverized under these conditions. This mechanism of dynamic gouge formation provides new insight to recent observations of the texture of gouge from the San Andreas fault-zone and from rupture zones in South African mines. Further, as such extreme conditions develop only during fast propagating earthquakes, presence or absence of pulverized gouge may serve as an indicator of earthquake propagation velocity.

Keywords: earthquakes; gouge; dynamic fracturing; faulting; San Andres

1. Introduction

A common feature of brittle fault-zones is grain-size reduction manifested by breccia and gouge formation. The fine-grain gouge that develops in central parts of fault-zones is believed to govern frictional properties of faults and the associated earthquake instability [1]. Reduction of grain-size is attributed to wear at points of contact (asperities) along the touching surfaces of two rock blocks due to local stress concentrations during shear displacement [2]. Bare rock surfaces quickly develop a gouge zone with progressive slip reaching thicknesses larger than the height of the asperities [3]. Thus, further grain-size reduction occurs by systematic grain crushing due to amplified grain-contact stresses [4] enhanced by the formation of "stress-

* Corresponding author. Tel.: +1 405 325 3157; fax: +1 405 325 3140.
E-mail addresses: reches@ou.edu (Z'. Reches), tdewers@ou.edu (T.A. Dewers).

0012-821X/$ - see front matter © 2005 Elsevier B.V. All rights reserved.
doi:10.1016/j.epsl.2005.04.009

chains" [5]. According to the grain-contact concept, cumulative slip along faults leads to continuous comminution and development of a self-similar particle size distribution [4]. The fractal dimension of 2.6–2.7 of the particle size distribution for several gouge zones [6,7] is in accord with the predictions of these models, with some exceptions [8].

While the above mechanisms assume quasi-static shear along pre-existing fault-zones, dynamic effects associated with fast propagating earthquakes were also considered. It was proposed that the high rate of implosive loading during earthquakes at dilational jogs of segmented faults could lead to brecciation [9]. Brune [10] suggested that fine-grain gouge along the San Andreas Fault formed by a cycle of unloading–loading of the normal stress across the fault during earthquakes. He attributed the unloading to tension associated with a slip pulse, which was observable experimentally [11].

We derive here a new model for the formation of fault gouge. The model is based on our recent analysis [12] of the gouge material of two faults from extremely different settings: the San Andreas Fault at Tejon Pass, California, and a new fault formed in a South African gold mine. We used these observations to bound the energetics of an earthquake, and to calculate the intense deformation conditions that can pulverize fault rocks at the tip of a propagating earthquake. In the analysis, we determine the deformation field close to the tip of a fast mode II fracture and discuss the effects of this field on the surrounding rocks.

2. Earthquake energetics and pulverized gouge

2.1. Fracture energy

Following Griffith's fracture model, the loading system of a fracture can be defined by its mechanical energy-release-rate, G, and the stress intensity factor, K; these parameters are related to each other as $G=K^2/E$ where E is Young's modulus (for plane stress and linear elastic solid). For a fracture propagating under equilibrium conditions, these parameters can be equated to the material resistance to fracturing that "consumes" the mechanical energy supplied by the loading system. The propagation of a fracture within an intact solid requires that the energy-release-rate should reach a critical value, G_C, which for a tensile fracture, equals 2γ where γ is the surface energy per unit area of the solid [13]. G_C is regarded as the fracture energy, which is a material property, and it corresponds to fracture toughness K_C.

Estimating the fracture energy, G_C, of a fast propagating earthquake is more complicated than the above relations for a slowly growing tensile fracture. The earthquake fracture energy accounts for at least three main energy consuming processes of the slipping fault: $G_C \approx U_S+U_F+E_S$, where U_S is the cumulative surface energy of gouge and new branches that form during the earthquake, U_F is the work done to overcome the fault frictional resistance (frictional heat), and E_S is the seismic (kinetic) energy of the accelerated particles [2]. In the section below, we use the observed gouge texture and fault structure to bound the fracture energy associated with an earthquake.

2.2. Gouge texture

We recently analyzed gouge material from two fault-zones [12]. One is the exhumed portion of the San Andreas Fault at Tejon Pass, California, where the fault-zone has accommodated at least 160 km of right-lateral displacement. We mapped the fault-zone and analyzed tens of samples collected within a 70–100 m wide zone of pulverized Cretaceous Tejon Lookout granite [14]. The second is the Bosman fault that formed during a $M=3.7$ 1997 earthquake in Hartebeestfontein gold mine, Klerksdorp, South Africa [15,16]. This is a new fault that formed in intact quartzite rocks during a single earthquake with maximum dip-slip of 0.37 m [15,16]. The quartzitic gouge of this fault was collected near focal depth of 2 km from the fault-zone that was exposed by mining about 1 yr after the earthquake.

We measured the texture of about 250 samples collected at both fault-zones using a laser particle size analyzer that provides a complete particle-size-distribution (PSD) in the 0.04–2000.00 μm range [12,14]. One of our central analytical objectives was to determine intrinsic gouge grain-size, as it was demonstrated that time-dependent aggregation/agglomeration of fine-grains may falsify the true PSD [12]. Some samples were analyzed continuously

in a circulating aqueous suspension for periods up to 190 h, showing progressive disaggregation into intrinsic grain-sizes ranging between 1.00 and 0.001 μm [12]. Thus the PSD obtained by previous workers (e.g. by mechanical sieving, optical methods, and quick measurements in a laser particle size analyzer) may be an inaccurate representation of true gouge texture.

The main results of the grain-size analyses are as follows (Fig. 1) [12]: (1) The gouge samples of the two fault-zones display similar texture (Fig. 1a); (2) The intrinsic PSD of the gouge merges after extended

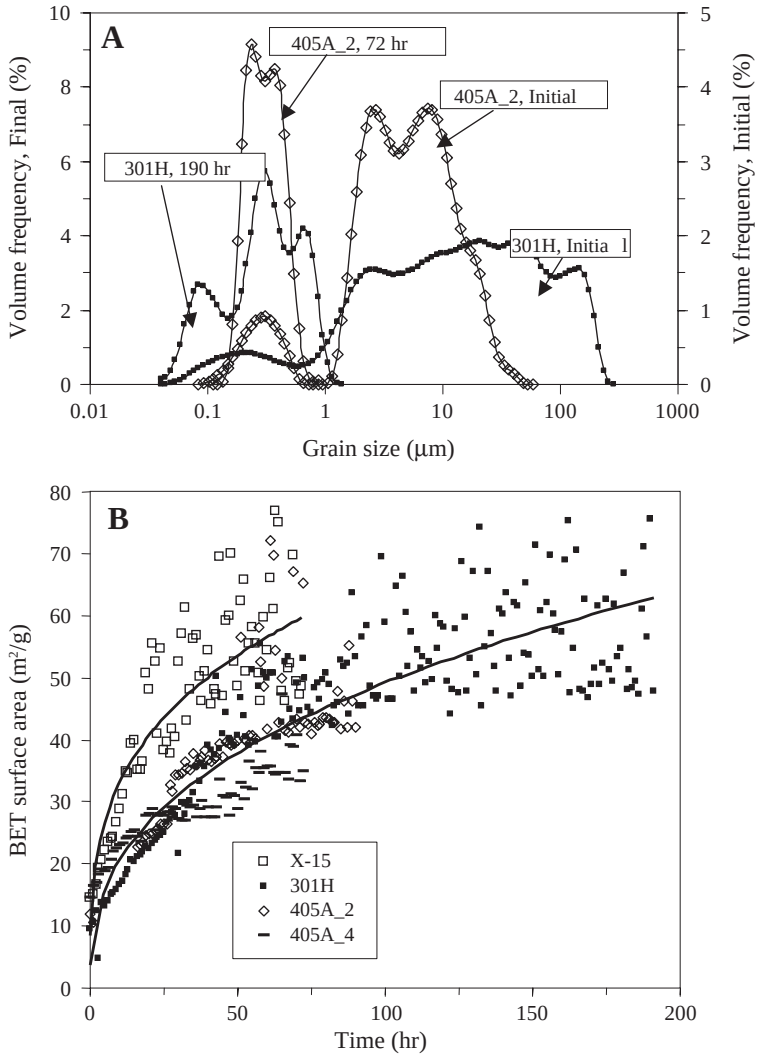

Fig. 1. Particle size distribution of two representative gouge samples measured for extended times in a laser particle size analyzer [12]. Samples are 301H, San Andreas Fault (solid squares) and 405A_2, Bosman Fault, Hartebeestfontein Mine, South Africa (open diamonds). A. Gouge grain-size distributions are shown as a percent of the total sample volume. Each sample is displayed by two curves, one for the initial stage (right axis), and one for the final stage (left axis). Only a small fraction of the initial distribution is smaller than 1 μm, whereas almost all grains of the final distribution are smaller than 1 μm. B. Changes in surface area with time resulting from disaggregation of four gouge samples including the two of A [12]. Samples X-15 and 301H are from the San Andreas Fault, and samples 405A_2 and 405A_4 are from Bosman Fault. Solid lines display a power–law relationship for the two longest disaggregation times. Surface areas of gouge approach 80 m^2/g, which is a significant contribution to the earthquake energy budget (see text).

running time (disaggregation time), and it reveals extreme fine size of 0.3 ± 0.2 μm (largest grains ~1.0 μm (Fig. 1a); (3) the BET surface area of the intrinsic gouge grains approaches 80 m^2/g, as was supported by SEM observations [12].

2.3. Fault-zone structure and earthquake energetics

The structure of the Bosman Fault and its gouge texture permit an estimation of its fracture energy G_C by using the above relations of $G_C \approx U_S + U_F + E_S$. The Bosman Fault contains tens of subparallel fractures that are ~1 mm thick and filled with the gouge characterized above (Fig. 1). As the surface area of the gouge formed by this earthquake reaches 80 m^2/g (Fig. 1b) [12], it corresponds to a surface energy of 0.2–0.36 MJ/m^2 for a 1 mm thick gouge zone. Summation of the surface energy within 10–30 fractures yields a total of $U_S = 2$–10 MJ/m^2 for this event.

The frictional work, $U_F = \tau \cdot d$, associated with this earthquake is estimated from the fault geometry. The Bosman Fault inclination is 60–70°, the 1997 earthquake slip is $d_{max} \sim 0.4$ m, and the vertical stress is $\sigma_v \sim 54$ MPa. If the horizontal stress obeys the Poisson effect for inactive tectonic regions ($\sigma_h \sim 18$ MPa), then the shear stress can be calculated yielding $U_F = 2.2$–3.0 MJ/m^2. Thus, in this earthquake, $U_F \leq U_S$, namely at least 50% of earthquake energy is invested in producing new gouge. As it is commonly accepted that the seismic energy, E_S, is only ~6% of the total energy [17], we ignore its contribution. Thus, the fracture energy of this earthquake is estimated as $G_C = 4$–13 MJ/m^2, where $G_C \approx U_F + U_S + E_S$.

This calculated range of fracture energy for the Bosman Fault, $G_C = 4$–13 MJ/m^2, falls in the range of energy-release-rates estimated for earthquakes, $G = 1$–100 MJ/m^2 [18]. It is important to note that these two ranges were determined independently. We now equate the loading energy (G) to the fracture energy ($G_C = G$), and assume that the calculated G_C for the Bosman Fault can serve as a bounding range for the energy-release-rate during this earthquake, namely $G = 4$–13 MJ/m^2.

2.4. Implications for gouge formation

The above observations provide three central constraints for gouge-forming models. First, the observed extremely fine-grain gouge requires appreciable energy to develop, suggesting a distinctive formation mechanism of the gouge. Second, the accurate determination of the gouge surface energy allows us to calculate a range of the fracture energy (G_C), and thus the energy-release-rate (G) of the $M = 3.7$ 1997 earthquake along the Bosman Fault. The third and most important point is the observation that gouges from the two fault-zones display strikingly similar particle-size-distributions (Fig. 1) [12]. This similarity appears in contrast to the profound differences between the two faults, and it leads us to deduce that gouge was formed by earthquake processes that are independent of the total amount of cumulative fault slip (160 km versus 0.37 m), sense of slip (strike-slip versus dip-slip), or rock type (granite versus quartzite). We postulate that the observed gouge production was controlled by the deformation conditions associated with a fast propagating earthquake, and to explore this option we derive these conditions below.

3. Deformation fields at the tip of a dynamic mode II fracture

3.1. Approach

The deformation fields for the tip of a mode II, two-dimensional fracture are determined here by using the asymptotic solution for an in-plane propagating fracture by Freund [19, Chap. 4], presented in the Appendix. The solution was derived for an isotropic elastic solid subjected to a fracture propagating at velocities smaller than C_R (Rayleigh wave velocity). These solutions were previously used to examine the branching process at the front of an earthquake rupture [20,21]. We consider sub-Rayleigh dynamic ruptures while noting that even higher propagation velocities, in the intersonic and supersonic range, were observed in laboratory experiments [22] and earthquakes [22,23].

3.2. Parameter selection and frames of reference

The parameters needed for the solutions belong to two groups, parameters that only weakly depend on the fracture propagation velocity and parameters that strongly depend on this velocity. For the first group

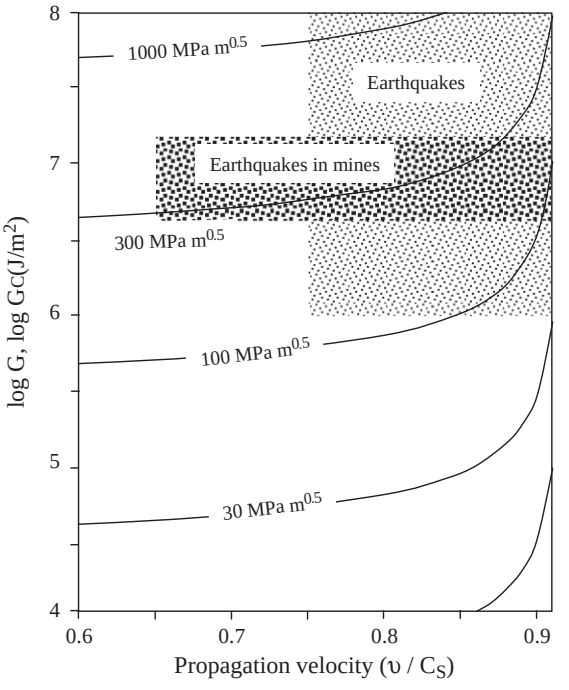

Fig. 2. The relations between energy-release-rate, G, and the stress intensity factor K_{II} of a dynamic mode II fracture as function of the fracture propagation velocity v/C_S (Eq. (3)). The contours indicate the values of K_{II} for the given G and v/C_S (see text). The shaded areas marked 'Earthquakes' and 'Earthquakes in mines' indicate the estimated ranges of G_C and v for earthquakes (see text).

we used typical values of a weak granite: density $\rho=2600$ kg m^{-3}, Poisson's ratio=0.22, and shear modulus $\mu=10$ GPa. The velocities of the compressional waves, C_d, shear waves, C_S, and Rayleigh waves, C_R, are the theoretical relations,

$$C_d=\sqrt{\frac{\mu+\lambda}{\rho}},\ C_s=\sqrt{\frac{\mu}{\rho}},\ \text{and}\ C_R=0.92C_s. \qquad (1)$$

The solutions depend weakly on the specific values of these parameters and we consider them as constants.

The second group of parameters includes the stress intensity factor K_{II} and the energy-release-rate G. For a planar, slowly propagating fracture in an infinite elastic solid, K_{II} is an indicator of the loading system

$$K_{II}=\tau(\pi L)^{0.5}\quad\text{and}\quad G=K_{II}^2/E \qquad (2)$$

where τ is the far-field shear stress and L is the fracture half-length. For a dynamic fracture, the relations depend on the propagation velocity [19, Eq. 5.3.10],

$$G=\frac{1+\upsilon}{2\mu}A_{II}K_{II}^2\qquad\text{where}\ A_{II}=\frac{v^2\alpha_s}{(1-\upsilon)\ C_S^2D} \qquad (3)$$

v is the fracture propagation velocity and the other variables are defined in the Appendix. The relations of Eq. (3) are mapped in Fig. 2, which displays contours of K_{II} in the space of G and v/C_S for the solid properties listed above. The two shaded regions marked as 'Earthquakes' and 'Earthquakes in mines' will be discussed later.

We use Freund's solutions to examine two components of the deformation that are likely to affect gouge formation: (1) strain rates (circumferential, radial, and dilation); and (2) stress intensity (maximum tensile and mean stress). The deformation is calculated in two reference frames. The first is the "fracture-tip frame" in which the deformation is presented with respect to the fracture tip as function of distance r and angle θ (Fig. 3). For a fracture propagating under uniform conditions, these parameters retain their shape and intensity with time. The second reference is the "medium-fixed frame" in which the deformation parameters are calculated for a fixed point $P(x_1, y_1)$ within the medium and away from the fracture (Fig. 3). In this reference frame the deformation parameters are calculated as a function of the time $t=(x/v)$ where x is the position of the fracture tip along its propagation axis, and v is the propagation velocity. We set $t=0$ for the time when the fracture tip is located at the shortest distance to the point, thus negative time indicates an approaching fracture tip and positive time indicates increasing distance of the fracture tip.

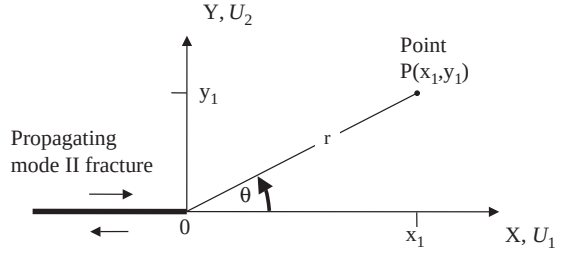

Fig. 3. Reference frames of the present analysis. The mode II fracture tip is at (0,0) and it propagates at velocity v in the positive X direction. The deformation states at the stationary point $P(x_1, y_1)$ are calculated for the relative position (r, θ) of the propagating fracture.

3.3. Results

3.3.1. Bounding the solutions

In the following calculations we use the theoretically derived relations (above and in the Appendix) to evaluate the deformation conditions at the tip region of a propagating mode II fracture. We use the accepted notion that the energy-release-rate, G, of a propagating fracture is equal to the fracture energy, G_C, of the host material [13]. The theoretical solutions are bounded by measurable physical parameters to facilitate their application to observations in the two fault-zones described above (and probably other). The bounds are based on the following estimates. First, the determined fracture energy values (G_C=4–13 MJ/m^2 for the Bosman Fault, and G_C=1–100 MJ/m^2 [18] for earthquakes in general) are used as bounding values of G, the energy-release-rate of the propagating fracture. Second, the estimated propagation velocities of earthquakes ($v=0.65\ C_s$ for earthquakes in gold mines [22], and $v>0.75\ C_s$ for earthquakes in general [23,24] are used as bounds on the fracture velocity. We use these estimates of G_C and v to plot the shaded regions in Fig. 2 that bound the ranges for two groups of the marked earthquakes. Finally, based of our observations that the typical width of a gouge bearing fracture that forms during an earthquake is 1–5 mm [15,16], we calculate the deformation conditions for distance of ± 3 mm around the fracture tip. It is assumed that the conditions calculated for this space represent the physical conditions at similar distance from the tip of a propagating earthquake.

The solutions for the deformation fields around the tip of the propagating mode II fracture are presented in two steps. The solutions are presented first by calculating the stress field and the strain-rate field for selected conditions and distances for the crack tip. We then present the full range of solutions relevant to earthquake propagation.

3.3.2. Fracture tip-fixed reference frame

For the calculation of the fracture-tip field, we select a fracture that propagates at $v=0.8\ C_s$ in a material with $G_C=6.7\cdot 10^4$ J/m^2; the associated stress intensity factor is $K_{II}=30$ MPa m$^{0.5}$. The fracture-tip deformation is presented by the angular variations ($-180^\circ<\theta<180^\circ$ of the radial strain rate, $\dot{e}_r$, the circumferential strain rate, $\dot{e}_\theta$, the two-dimensional dilation rate, $\dot{e}_d=\dot{e}_r+\dot{e}_\theta$ (Fig. 4a), the maximum tensile stress σ_1, and the mean stress $(\sigma_1+\sigma_2)/2$ (Fig. 4b). The plotted results are for $r=3$ mm (distance from the fracture tip) for a fracture propagating at a velocity $v=0.8\ C_S$ with the properties listed in the caption. This distance of 3 mm is selected as the typical observed width of the gouge zone in the Bosman fault-zone [16].

Fig. 4 reveals that $\dot{e}_r$ and $\dot{e}_\theta$ alternate their signs between tensile (positive) strain rate and compressive (negative) strain rate around the fracture tip. There are four cycles of the dilation rate, $\dot{e}_d$, that alternates between volumetric expansion (sectors -48° to -100°, -135° to -180°, 0–57°, and 110–143°, and volumetric contraction (sectors -0° to -48°, -100° to -135°,57–110°, and 143–180° (Fig. 4a). Locally, $\dot{e}_d$ magnitude approaches the magnitude of the most tensile strain rate; e.g., at $\theta\sim 80^\circ$ (Fig. 3a). In Fig. 4b the maximum stress, σ_1, is tensile in a large sector of $-180^\circ<\theta<60^\circ$, and even the mean stress, $(\sigma_1+\sigma_2)/2$, is tensile for $-180^\circ<\theta<0^\circ$. This tensile deformation, and particularly the frequent alternation between expansion and contraction, is a favorable condition for rock fragmentation into gouge as discussed later.

3.3.3. Medium-fixed reference frame

We now consider the deformation at two fixed points within the medium located at $Y=\pm 3$ mm on both sides of the fracture surface (Fig. 3). The presented parameters are the maximum tensile stress, σ_1, and the two-dimensional dilation rate, $\dot{e}_d$ (Appendix). The time variations of these parameters are shown for a period during which the fracture tip approaches the points. We now consider a fracture propagating at $v=0.91\ C_S$ in a material with $G_C=9.1\cdot 10^5$ J/m^2; the associated stress intensity factor is $K_{II}=30$ MPa m$^{0.5}$. Fig. 5 exhibits rapid intensity changes of the maximum stress and dilation rate as the fracture approaches the reference point. Most of the changes occur in the time range of $-1<t<1$ μs that corresponds to distance range of $-1.8<r<1.8$ mm.

The most important features in Fig. 5 are the extreme values of the stress and the dilation rate. The figure shows that σ_1 is true tensile in $Y<0$ for the complete time span, and σ_1 is true tensile in $Y>0$ for $t<0$, namely before the fractures tip passes at its shortest distance. The intensity of σ_1 increases strongly with proximity to the fracture tip and it

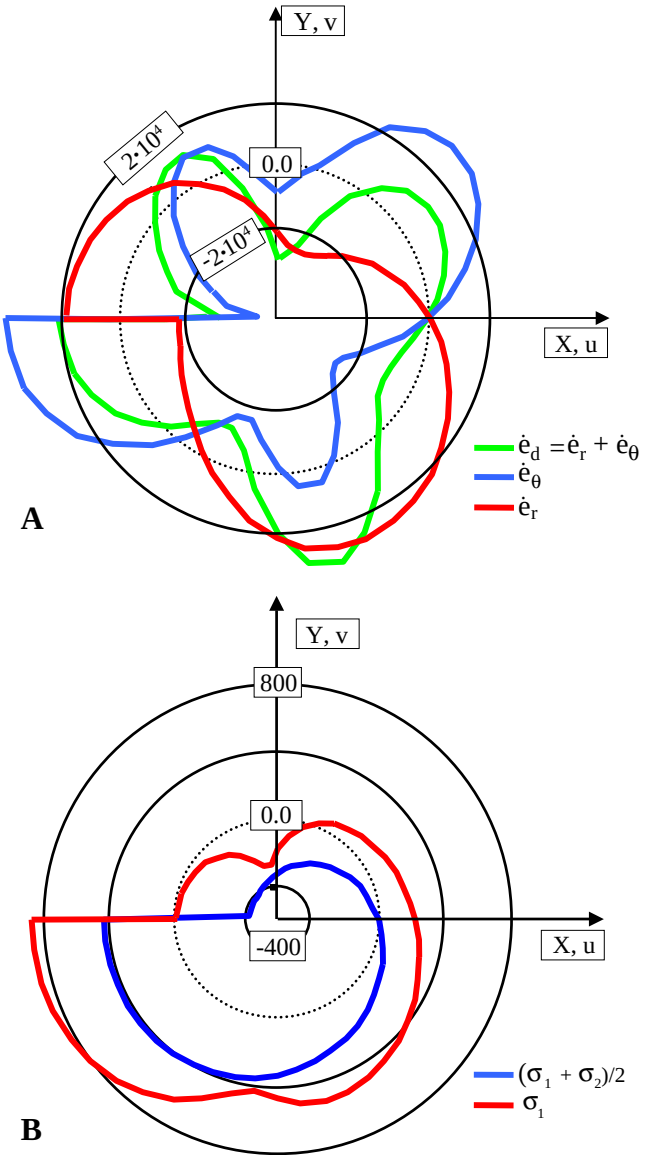

Fig. 4. Deformation fields around the tip of a propagating mode II fracture in the fracture-tip frame of reference; equations are presented in the Appendix. The shown results are for $v=0.8\ C_S$, $r=3$ mm, and rock properties of $\rho=2600$ kg m^{-3}, $\nu=0.22$, $\mu=10$ GPa, and $K_{II}=30$ MPa m$^{-0.5}$ (see text). A. Radial plot of the intensity of the strain rates (radial, $\dot{e}_r$, circumferential, $\dot{e}_\theta$, and dilation, $\dot{e}_d$); dotted circle indicates vanishing strain rates (e.g. at $\theta=0^\circ$). Note four sectors in which the dilation rate is tensile (positive). B. Radial plot of the intensity of the maximum tensile stress, σ_1, and the mean stress, $(\sigma_1+\sigma_2)/2$; solid circle indicates vanishing stresses. Note that the mean stress is tensile (positive) for all the region of $\theta<0$.

exceeds 10 GPa at $t\sim0.5$ μs (Fig. 5a). The dilation rate is expansion for $Y<0$ and it approaches 10^6 s^{-1} during $-0.4<t<0$ μs (Fig. 5b). The dilation rate is contraction for $Y>0$ and $t>0$, and it approaches $-9\cdot1^5$ s^{-1} during $-0.3<t<0.1$ μs. Further, these extreme dilation rates rapidly invert their sense from expansion to contraction in $Y<0$, and from contraction to expansion in $Y>0$ (Fig. 5b). The inversion occurs during a period shorter than about 1 μs indicating that the rocks on both sides of the propagating

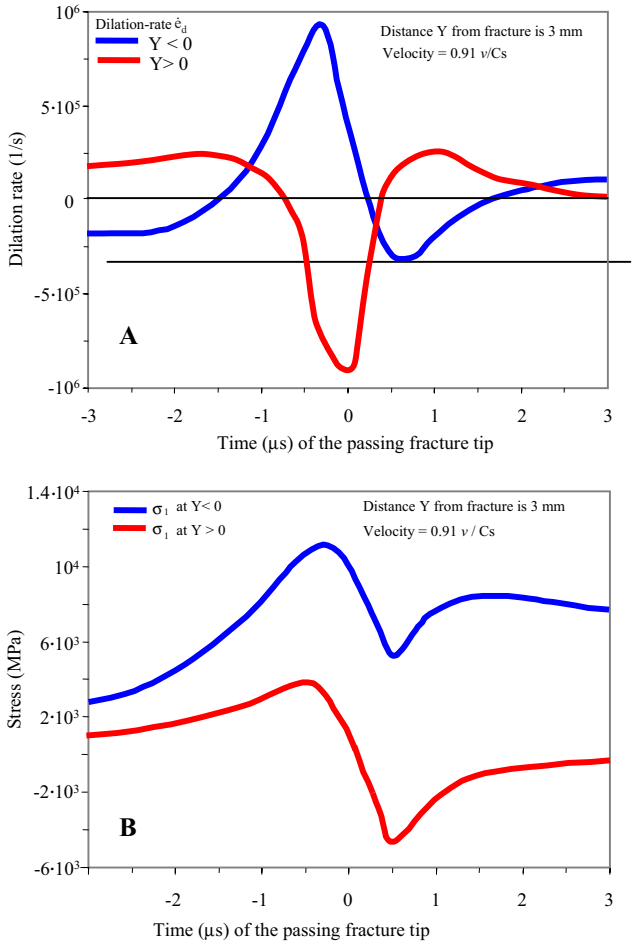

Fig. 5. Time variations of rock deformation at medium frame of reference close to a dynamic mode II fracture. System geometry appears in Fig. 3; fracture velocity is $v=0.91\ C_S$; calculated for two points that are located at distance of 3 mm from both sides of the propagating fracture ($Y<0$ and $Y>0$); results are shown as function of time (μs) where $t=0$ when the fracture tip is at the shortest distance from the stationary point ($r=3$ mm for this case); at this velocity, 1 μs~3.1 mm for the given rock properties. A. The maximum tensile stress, σ_1, plotted as a function of time; note that σ_1 is tensile for the entire time in the $Y<0$ region, and it is tensile for $t<0$ in the $Y>0$ region. B. The dilation rates; note that the alternation between maximum volumetric expansion and maximum volumetric contraction occurs in less than 1 μs.

fracture are subjected to a cycle of intense expansion and contraction.

3.3.4. *Extreme deformation conditions at the tip region*

The complete range of deformation parameters are mapped in Fig. 6 in the space of G and v/C_S (same as in Fig. 2). Fig. 6 also displays the parameter bounds of earthquakes as discussed above. The map in Fig. 6a displays the maximum tensile stress, σ_1, at distance of $r=3$ mm and $\theta=-180^\circ$ with respect to the fracture tip. According to Fig. 4a, the maximum tension occurs at this angle. Fig. 6b is the map of the maximum dilation rate, $\dot{e}_d$, for $r=3$ mm and $\theta=-75^\circ$; at this angle the dilation rate reaches its maximum value (Fig. 4b). Due to anti-symmetry of the stress field of a mode II fracture, Fig. 6a also represents the absolute value of the maximum compression, σ_3, for $r=3$ mm and $\theta=-180^\circ$ (Fig. 4a).

Fig. 6 indicates profound increase of stress intensity and dilation rates with propagation velocity (note logarithmic contour intervals). For example, the max-

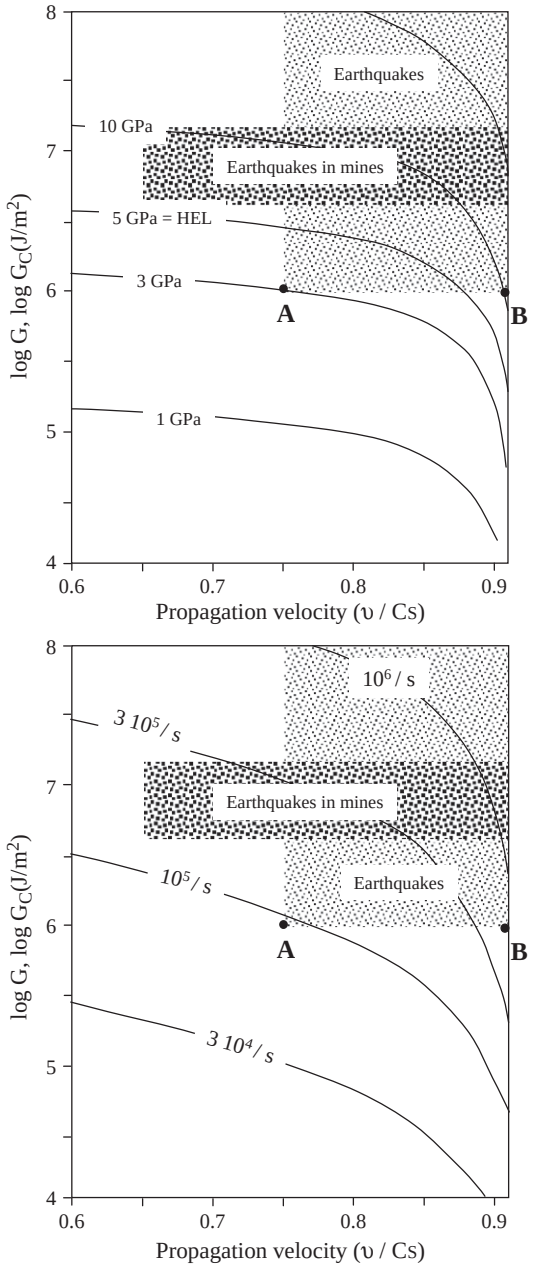

Fig. 6. The deformation conditions at the tip region of a propagating mode II fracture as displayed for the space of energy-release-rate G, and propagation velocity v/C_S, similarly to Fig. 2. The calculations are for distance of 3 mm from the tip and rock properties of $\rho=2600$ kg m^{-3}, $\nu=0.22$, $\mu=10$ GPa. A. Contours of maximum tensile stress σ_1, calculated for $\theta=180^\circ$ (see Fig. 4b). B. Contours of maximum dilation rates (s^{-1}) calculated for $\theta=180^\circ$ (see Fig. 4a). The shaded regions indicate the range of calculated G_C for earthquakes and the common propagation velocities of earthquakes (see text).

imum tension is ~3 GPa for a fracture propagating at $v=0.75\ C_S$ in a material with $G_C=1$ MJ/m^2 (point A, Fig. 6a) and the stress is larger than 10 GPa for $v=0.91\ C_S$ (point B, Fig. 6a). Both these values are for the same distance of $r=3$ mm, and higher values exist at shorter distances. The corresponding dilation rates are extreme: $\dot{e}_d \sim 9\cdot 10^4$ s^{-1} for $v=0.75\ C_S$ (point A, Fig. 6b) that increases to $\sim 4\cdot 10^5$ s^{-1} for $v=0.91\ C_S$ (point B, Fig. 6b).

In summary, the solutions indicate:

1. Intense tensile stresses develop within a zone of ~6 mm width around the tip of a fast propagating fracture. In this zone, σ_1 exceeds 3 GPa for fractures that propagate at $v>0.75\ C_S$ and $G>1$ MJ/m^2 (shaded region marked 'Earthquakes' in Fig. 6).
2. The dilation rates develop a zone of a few millimeters width around the fracture tip alternating between expansion and contraction as the fracture tip passes. The extreme dilation rates exceed 10^5 s^{-1} for fractures that propagate at $v>0.75\ C_S$ and $G>1$ MJ/m^2 (shaded region marked 'Earthquakes' in Fig. 6).
3. The deformation intensity depends strongly on the propagation velocity and distance to tip: the high deformation intensity is restricted to a distance of 1–3 mm from the tip of a fracture with $v>0.75\ C_S$.

4. Model for gouge pulverization by earthquake rupture

4.1. Rock pulverization at the earthquake tip

The calculations show that the deformation conditions within the tip region (~6 mm wide) of a dynamic mode II fracture are comparable in intensity (stress intensity and strain rates) to the deformation conditions that develop during shock impacts [25–27]. It was documented that the intense deformation associated with extraterrestrial impacts cause fragmentation, melting, and evaporation close to the impact site, and plastic deformation and fracturing away from the site [25]. The transition from elastic state to failure occurs when the stress exceeds the Hugoniot Elastic Limit (HEL) of the rock. In experiments, the HEL is identified as the point of deviation from linear pressure–volume of the elastic solid in shock conditions

[25]. When the HEL is exceeded the activated failure mechanisms (e.g. fracturing, plastic flow, formation of planar-deformation-features) decrease the rock density and mobilize plastic flow. The approximate HEL of granite is 5 GPa [27], and this value is contoured in Fig. 6a.

We now propose that the extreme deformation conditions at the tip region of an earthquake rupture could pulverize fault rocks and generate the observed fine-grain gouge. The process is schematically displayed in Fig. 7, showing alternating dilation rates within the $Y<0$ side of the rupture after Fig. 5b. When the rupture tip is far from a stationary point in the rock, stage I in Fig. 7 at a distance larger than 10 mm for the given conditions, the dilation rates are too small to fragment the solid rock. At a distance of about 1–3 mm, the dilation rates exceed 10^5 s^{-1} and the solid rock could be fragmented under expansion (stage II in Fig. 7). After less than 1 μs the volumetric expansion is inverted into contraction leading to further fragmentation of the newly formed granular material (stage III, Fig. 7b).

The extreme stress (exceeding HEL), the intense dilation rates, and the alternations of volumetric strain are all likely contributors to the pulverization of the fault rocks. It is well known that the fracturing style of brittle solids is strongly affected by the loading rate [28]. Under quasi-static loading, the solid fails initially at its weakest point, and the growing fracture relaxes tensile stresses within a large volume. This process forms few, long, sparsely spaced, and subparallel fractures. On the other hand, under dynamic

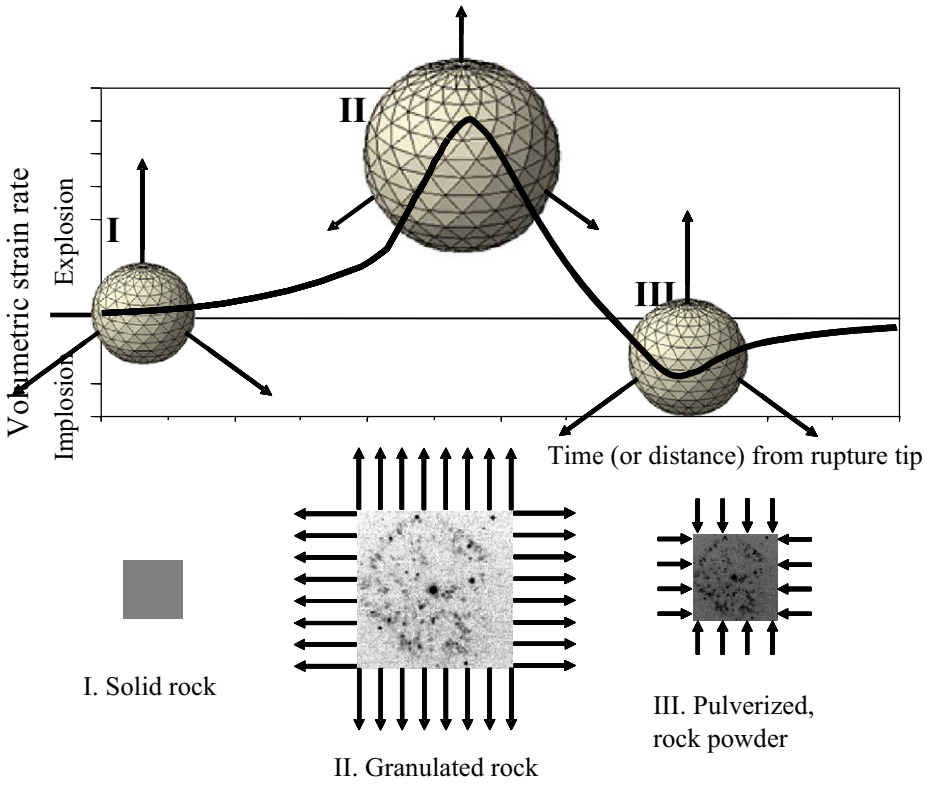

Fig. 7. The proposed model for gouge formation by rupture front fragmentation during fast propagating earthquakes. Upper diagram presents the time variations of the dilation rates at the rock at $Y<0$ as the rupture tip approaches it and passes by it (schematically after Fig. 5b). We recognize three stages. Stage I: The rupture front is far, and it induces only negligible expansion of the rocks that remain solid. Stage II: Maximum expansion rate, which can exceed 10^5 s^{-1}, leads to pervasive fragmentation (possible mechanisms analyzed by Grady and Kipp [28]. Stage III: Maximum contraction rate that further pulverizes the granular material of stage II (e.g. by mechanisms discussed by Nesterenko [30]. In the region of $Y>0$, the fragmentation–pulverization cycle starts with contraction that alternates into expansion (Fig. 5b).

loading, failure initiates at many, closely spaced points, and multiple fractures grow simultaneously. Each of these fractures relaxes the tensile stress within a small volume [28] forming many, short, closely spaced crosscutting fractures, leading to fragmentation of the solid.

The mechanics of solid fragmentation under dynamic expansion was examined by Grady and Kipp [28]. Their analysis assumes that the solid disintegrates into many particles that move away from the mass center. At high velocity of the particles, the system energy is dominated by two components: the kinetic energy of the particles, which is proportional to the loading rate, and the surface energy of the particles, which is proportional to their size,

$$U = \frac{3}{10}\frac{\dot{\rho}^2}{\rho A^2} + \gamma A$$

where A is the mean particle surface area, ρ and $\dot{\rho}$ are the density and rate of density change, and γ is the specific surface energy. Grady and Kipp [28] show that the mean grain-size, d, could be predicted by the following relations,

$$d = \left[\frac{\sqrt{20}K_{IC}}{\rho C_d \dot{e}}\right]^{2/3} \quad (4)$$

where K_{IC} is the mode I fracture toughness and C_d is the compressive wave velocity. The last equation was successful in predicting grain-size in fragmentation experiments with oil shale under conditions leading to dynamic expansion [28].

Fragmentation also occurs under contraction loading of granular material. Under quasi-static contraction, brittle grains fail by fracturing when the stresses at grain contacts exceed compressive strength, as observed experimentally [29]. Dynamic contraction loading may activate several complex failure mechanisms including grain fracturing, void collapse, plastic flow, grain-contact sliding, heating or melting [30]. This complexity of failure mechanisms was demonstrated, for example, in the explosion experiments of granular SiC samples producing grain-size reduction, shear band formation and local melting [30]. The relationship between grain-size and strain rate is unknown for dynamic contraction probably due to the process complexity.

4.2. Implications

The model proposed above is based on the following steps:

I. The analyses of seismic and rock mechanics observations indicate that the fracture energy of earthquakes is in the range of $G_C = 1$–100 MJ/m^2 [18], and that earthquakes propagate at velocities exceeding ~0.75 the shear wave velocity [22,23].
II. The present analysis calculates the deformation at the tip of a mode II fracture that propagates under these values of fracture energy and velocity. It is shown that extreme deformation conditions develop in a zone of a few millimeters width around the fracture tip.
III. We propose that the extreme conditions at the earthquake tip (the process zone) pulverize the fault rocks.

One outstanding result of the calculations is the strong dependence of the tip conditions on the propagation velocity (Fig. 6 and related discussion). We consider now an earthquake that propagates within a fault-zone of uniform composition, which would indicate constant fracture energy, G_C. The propagation velocity may vary along the path due to complex variations in loading, geometry, branching and slip history. We demonstrate in the following paragraph that the intensity of fault rock pulverization can indicate the local propagating velocity.

In the studies of earthquake rupture zones at focal depth in South Africa mines, we analyzed the rupture zones of three earthquakes [15,16] that profoundly differ in the amounts of the produced pulverized rock powder. The 1997 $M = 3.7$ event in the Hartebeestefontein mine (the Bosman Fault described above) produced huge amounts of pulverized rock powder with sub-micron grains while breaking intact rocks and forming a new fault-zone. The $M = 4.3$ earthquake that occurred in 2001 along the 5Shaft fault in ARM-5 mine near Klerksdorp, South Africa, displayed slip along multiple preexisting fractures within a preexisting wide fault-zone with at least 320 m of cumulative displacement. This earthquake produced only a negligible amount of rock powder. The third event is the 1999 $M = 4.6$ Matjhabeng earthquake in Welkom area, which occurred along the Dagbreek Fault with cumu-

lative slip of a few kilometers [15]. The intensity of rock rupturing and in particular the amount of newly formed gouge powder, varied from highly abundant at a few sites to negligible amounts in others [15,16]. These three earthquakes occurred under similar loading (mining-induced normal faulting), and within the similar host rocks (brittle quartzite). We thus attribute the differences in pulverization intensity to differences in propagation velocities between these earthquakes, and deduce that the 1997 $M=3.7$ earthquake propagated at the highest velocity.

Finally, it was proposed recently that the gouge-zones of large faults undergo cyclical changes during and subsequent to each large earthquake [31,32]. This cycle includes intense fragmentation during the earthquake followed by cementation during the interseismic stage that strengthens the fault-zone. The extreme dilation rates calculated here could serve as the mechanism of dynamic pulverization at the rupture tip that generates highly chemically reactive powdered gouge to be cemented, as part of this cycle, in association with fault-zone fluids [32,33].

5. Summary

We examine the deformation conditions at the tip of a dynamic rupture that propagates at a magnitude of velocity approaching the Rayleigh wave speed. We found that extreme tensile stresses and rates of volumetric expansion and volumetric contraction exist at short distances from the tip of such dynamic ruptures. Previous theoretical and experimental analyses indicate that such extreme dynamic conditions cause pervasive fragmentation of brittle solids and granular materials. We propose that a fast propagating earthquake rupture pulverizes fault rocks and forms fine-grain gouge. The model suggests that a 1–3 mm thick gouge zone would form during a single earthquake if the rupture propagates near or at Rayleigh wave velocity, regardless of shear displacement across the gouge zone. It is proposed that evidence for such pulverization can be used to estimate the propagation velocity of past earthquakes.

The present model is based on an analytical solution for a sharp-tip fracture within an elastic solid. We envision that the calculated singular deformation field could activate a range of nonlinear, irreversible mechanisms such as the pulverization discussed here, as well as plastic deformation, phase transformations and melting [e.g., 28]. These mechanisms lead to the development of a process zone in front of an earthquake rupture that facilitates the rupture propagation.

Acknowledgments

We wish to thank Brent Wilson and Sam Goeppenger who contributed expertise in grain-size analysis, Ory Dor, Koos Bosman and Gerrie van-Aswegen for help in working in the gold mines of South Africa, and Jim Brune, Yehuda BenZion, Amir Sagy and Jay Fineberg for insightful discussions in the field and elsewhere. The comments of the anonymous reviewers greatly contributed to the improvement of the paper.

The study was supported by the U.S. National Science Foundation, grant EAR0207847, US-Israel BiNational Fund, grant 98-135, and by Israel Science Fund, grant 175-02.

Appendix A

The deformation fields associated with a dynamic mode II fracture are calculated for two reference systems (see text): the "fracture tip-fixed frame" with respect to the fracture tip, and the "medium-fixed frame" with respect to a fixed point in the medium away from the fracture (Fig. 3). For both systems, we used the relations derived by Freund [19]. The stresses at point $P(r, \theta)$ with respect to the tip of a propagating mode II fracture are [19, Eqs. 4.3.23–25]

$$\sigma_{ij} = \frac{K_{\mathrm{II}}}{\sqrt{2\pi r}} \sum_{ij}^{\mathrm{II}} (\theta, v) \tag{1a}$$

where

$$\sum_{11}^{\mathrm{II}} = -\frac{2\alpha_s}{D}\left[\left(1+2\alpha_d^2-\alpha_s^2\right)\frac{\sin 0.5\theta_d}{\sqrt{\gamma_d}} - \left(1-\alpha_s^2\right)\frac{\sin 0.5\theta_s}{\sqrt{\gamma_s}}\right] \tag{1b}$$

$$\sum_{12}^{\mathrm{II}} = \frac{1}{D}\left[4\alpha_d\alpha_s\frac{\cos 0.5\theta_d}{\sqrt{\gamma_d}} - \left(1+\alpha_s^2\right)^2\frac{\cos 0.5\theta_s}{\sqrt{\gamma_s}}\right] \tag{1c}$$

$$\sum_{22}^{II} = \frac{2\alpha_s\left(1+\alpha_s^2\right)}{D}\left[\frac{\sin 0.5\theta_d}{\sqrt{\gamma_d}} - \frac{\sin 0.5\theta_s}{\sqrt{\gamma_s}}\right] \quad (1d)$$

and

$$D = 4\alpha_d\alpha_s - \left(1+\alpha_s^2\right)^2$$

$$\alpha_d = \sqrt{1 - v^2/C_d^2}$$

$$\alpha_s = \sqrt{1 - v^2/C_s^2}$$

$$\gamma_d = \sqrt{1 - (v\sin\theta/C_d)^2}, \qquad \tan\theta_d = \alpha_d\tan\theta$$

$$\gamma_s = \sqrt{1 - (v\sin\theta/C_s)^2}, \qquad \tan\theta_s = \alpha_s\tan\theta$$

where v is the fracture propagation velocity, K_{II} is the temporary mode II stress intensity factor, μ is the shear modulus of the elastic body, and C_S and C_d are the velocities of the shear waves and compressional waves of this body, respectively. The particle velocities at point, $P(r, \theta)$ are

$$\dot{u}_1 \approx \frac{v\alpha_s K_{II}}{\mu D\sqrt{2\pi r}}\left[2\frac{\sin 0.5\theta_d}{\sqrt{\gamma_d}} - \left(1+\alpha_s^2\right)\frac{\sin 0.5\theta_s}{\sqrt{\gamma_s}}\right] \quad (2a)$$

$$\dot{u}_2 \approx -\frac{v\alpha_s K_{II}}{\mu D\sqrt{2\pi r}}\left[2\alpha_d\alpha_s\frac{\cos 0.5\theta_d}{\sqrt{\gamma_d}} - \left(1+\alpha_s^2\right)\frac{\cos 0.5\theta_s}{\sqrt{\gamma_s}}\right] \quad (2b)$$

For calculations in the "fracture-tip frame", we converted the above stresses and velocities to their polar coordinate equivalents

σ_{rr}, $\sigma_{\theta\theta}$, $\sigma_{r\theta}$, $\dot{u}_r$, and $\dot{u}_\theta$

by using standard transformation relations. The polar strain rates are calculated from the relations

$$\dot{e}_r = \frac{\partial \dot{u}_r}{\partial r} \quad (3a)$$

$$\dot{e}_\theta = \frac{\dot{u}_r}{r} + \frac{1}{r}\frac{\partial \dot{u}_\theta}{\partial \theta} \quad (3b)$$

The "medium-fixed frame" uses a medium reference system (x, y) in which the $y=0$ axis coincides with the fracture surface (Fig. 3). The deformation is calculated at a fixed point $P(x_1, y_1)$ as the fracture approaches it and passes by it. Unlike the "fracture-tip frame" where the deformation at $P(r, \theta)$ are time-independent, here the r and θ values of point $P(x_1, y_1)$ change with time, and one should consider $P(r, \theta, t)$. As mentioned in the text, the time is $t=(x/v)$ where x is the position of the fracture tip along its propagation axis, and v is the propagation velocity (Fig. 3). For the medium-fixed frame, we calculated the maximum extension rate, maximum contraction rate, and dilation rate from the rates of the principal stresses σ_1 and σ_2,

$$\dot{e}_1 = \frac{\dot{\sigma}_1}{E} \quad (4a)$$

$$\dot{e}_2 = \frac{\dot{\sigma}_2}{E} \quad (4b)$$

$$\dot{e}_d = \dot{e}_1 + \dot{e}_2 \quad (4c)$$

where E is Young's modulus.

References

[1] Y. Ben-Zion, C.G. Sammis, Characterization of fault zones, Pure Appl. Geophys. 160 (2003) 677–715.

[2] C.H. Scholz, The Mechanics of Earthquakes and Faulting, Cambridge University Press, London, 2002, 471 pp.

[3] R.A. Yund, M.L. Blanpied, T.E. Tullis, J.D. Weeks, Amorphous material in high strain experimental fault gouges, J. Geophys. Res. 95 (1990) 15589–15602.

[4] C.G. Sammis, R.H. Osborne, J.L. Anderson, M. Banerdt, P. White, Self-similar cataclasis in the formation of fault gouge, Pure Appl. Geophys. 124 (1986) 53–78.

[5] J.K. Morgan, Particle dynamics simulations of rate- and state-dependent frictional sliding of granular fault gouge, Pure Appl. Geophys. 161 (2004) 1877–1891.

[6] S.J. Steacy, C.G. Sammis, An automaton for fractal patterns of fragmentation, Nature 353 (1991) 250–252.

[7] L.J. An, C.G. Sammis, Particle-size distribution of cataclastic fault materials from southern California—a 3-d study, Pure Appl. Geophys. 143 (1994) 203–227.

[8] C. Marone, C.H. Scholz, Particle-size distribution and microstructures within simulated fault gouge, J. Struct. Geol. 11 (1989) 799–814.

[9] R.H. Sibson, Brecciation processes in fault zones; inferences from earthquake rupturing, Pure Appl. Geophys. 124 (1986) 159–175.

[10] J.N. Brune, Fault-normal dynamic unloading and loading: an explanation for "non-gouge" rock powder and lack of fault-

parallel shear bands along the San Andreas Fault, EOS Trans. AGU 82 (47) (2001) (Fall Meet. Suppl., Abstract S22B-0655).
[11] A. Anooshehpoor, J.N. Brune, Frictional heat-generation and seismic radiation in a foam rubber model of earthquakes, Pure Appl. Geophys. 142 (1994) 735–747.
[12] B. Wilson, T. Dewers, Z. Reches, J. Brune, Particle size and energetics of gouge from earthquake rupture zones, Nature, in press.
[13] B. Lawn, Fracture of Brittle Solids, Cambridge Univ. Press, 1993, 378 pp.
[14] B. Wilson, Meso- and Micro-structural Analysis of the San Andreas Fault at Tejon Pass, California Unpublished Masters Thesis, University of Oklahoma, Norman, Oklahoma, 2004, 279 pp.
[15] O. Dor, Z. Reches, G. van Aswagen, Fault zones associated with the Matjhabeng earthquake 1999, South Africa, Rockburst and Seismicity in Mines, RaSiM5 (Proceedings), South African Inst. of Mining and Metallurgy, 2002, pp. 109–112.
[16] O. Dor, Z. Reches, G. van Aswagen, K. Bosman, Earthquake rupture at the focal depth earthquakes in gold mines, South Africa, EOS Trans. AGU 82 (47) (2001) (Fall Meet. Suppl., Abstract S52B-0626).
[17] A. McGarr, On relating apparent stress to the stress causing earthquake fault slip, J. Geophys. Res. 104 (1999) 3003–3011.
[18] V.C. Li, Mechanics of shear rupture applied to earthquake zones, in: B.K. Atkinson (Ed.), Fracture Mechanics of Rocks, Academic Press, London, 1987, pp. 351–428.
[19] L.B. Freund, Dynamic Fracture Mechanics, Cambridge Univ. Press, 1990, 563 pp.
[20] A.N.B. Poliakov, R. Dmowska, J.R. Rice, Dynamic shear rupture interactions with fault bends and off-axis secondary faulting, J. Geophys. Res. 107 (B11) (2002) (Art. 2295).
[21] N. Kame, T. Yamashita, Dynamic branching, arresting of rupture and the seismic wave radiation in self-chosen crack path modeling, Geophys. J. Int. 155 (2003) 1042–1050.
[22] T. Yamada, J.J. Mori, S. Ide, H. Kawakata, Y. Iio, H. Ogasawara, Radiation efficiency and apparent stress of small earthquakes in a South African gold mine, J. Geophys. Res. 110 (B01305) (2005).
[23] K. Xia, A.J. Rosakis, H. Kanamori, Laboratory earthquakes: the sub-Rayleigh-to-supershear rupture transition, Science 303 (2004) 1859–1861.
[24] S. Das, Dynamic fracture mechanics in the study of the earthquake rupturing process: theory and observation, J. Mech. Phys. Solids 51 (2003) 1939–1955.
[25] H.J. Melosh, Impact Cratering: a Geologic Process, Oxford Univ. Press, 1989, 245 pp.
[26] A. Sagy, Z. Reches, J. Fineberg, Dynamic fracture by large extraterrestrial impacts as the origin of shatter cones, Nature 418 (2002) 310–313.
[27] D.E. Grady, N.A. Winfree, Impact fragmentation of high-velocity compact projectiles on thin plates: a physical and statistical characterization of fragment debris, Int. J. Impact Eng. 26 (2001) 249–262.
[28] D.E. Grady, M.E. Kipp, Dynamic rock fragmentation, in: B.K. Atkinson (Ed.), Fracture Mechanics of Rocks, Academic Press, London, 1987, pp. 429–475.
[29] T. Dewers, A. Hajash, Rate laws for water-assisted compaction and stress-induced water–rock interaction in sandstones, J. Geophys. Res. 100 (1995) 13093–13112.
[30] V.F. Nesterenko, Dynamics of Heterogeneous Materials, Springer, 2001, 510 pp.
[31] Z. Reches, Mechanisms of slip nucleation during earthquakes, Earth Planet. Sci. Lett. 170 (1999) 475–486.
[32] S.K. Muhuri, T.A. Dewers, T.E. Scott, Z. Reches, Interseismic fault strengthening and earthquake slip instability: friction or cohesion? Geology 31 (2003) 881–884.
[33] T.A. Dewers, Z. Reches, Alteration of fresh fault gouge from focal depths of recent earthquakes in deep mines, Eos Trans. AGU 85 (47) (2004) (Fall Meet. Suppl., Abstract S41B-0969).